

# Phase field simulations of coupled microstructure solidification problems via the strong form particle difference method

Jeong-Hoon Song  · Yao Fu · Tae-Yeon Kim · Yeong-Cheol Yoon ·  
John G. Michopoulos · Timon Rabczuk

Received: 8 June 2017 / Accepted: 31 August 2017 / Published online: 8 September 2017  
© Springer Science+Business Media B.V. 2017

**Abstract** This paper presents the development of a strong form-based collocation method called the particle difference method (PDM), capable of predicting the spatiotemporal evolution of polycrystalline material solidification through coupling of multi-phase and temperature fields. Cross coupled phase field evolution and heat transfer equations are discretized via the PDM to obtain the interface kinematics of polycrystalline boundary during solidification. A distinct feature of the PDM is its ability to represent derivative operators via a moving least-square approximation of the Taylor expansion through point-wise computations at collocation points. The method discretizes directly the strong forms using the pre-computed derivative operators at each collocation point and elegantly overcomes the topological difficulty in modeling intricate moving interfaces. To

verify the efficacy of the PDM, numerical results are compared with those obtained from the conventional finite difference method for uniform and irregular distributions of the collocation points. The scalability of the parallelized PDM is tested by measuring its efficiency with increasing the number of processors. We also provide a solidification simulation with two ellipsoidal inclusions to demonstrate the capability of the PDM in complex moving interface problems with high curvature.

**Keywords** Microstructure · Polycrystalline · Solidification · Phase field model · Strong form · Point collocation

---

J.-H. Song (✉)  
Department of Civil, Environmental and Architectural  
Engineering, University of Colorado at Boulder, Boulder,  
CO 80309, USA  
e-mail: jh.song@colorado.edu

Y. Fu  
Department of Aerospace Engineering and Engineering  
Mechanics, University of Cincinnati, Cincinnati,  
OH 45220, USA

T.-Y. Kim  
Civil Infrastructure and Environmental Engineering,  
Khalifa University of Science and Technology,  
Abu Dhabi 127788, UAE

Y.-C. Yoon  
Department of Civil Engineering, Myongji College,  
Seoul 120-776, South Korea

J. G. Michopoulos  
Computational Multiphysics Systems Laboratory, Naval  
Research Laboratory, Washington, DC 20357, USA

T. Rabczuk  
Institute of Structural Mechanics, Bauhaus-University  
Weimar, Marienstrasse 15, 99423 Weimar, Germany

## 1 Introduction

The prediction of microstructural evolution during solidification, recrystallization, and phase transformation processes has attracted intense interest due to the plethora of relevant applications, especially in material manufacturings such as casting, welding, sintering and the recently emerging fields of additive manufacturing technologies. The phase-field model (PFM) has been proven as one of the most popular and powerful approaches among various modeling approaches for these problems. Following the seminal work by Karma (2001) on the prediction of dendritic alloy solidification, the PFM has appeared as an effective approach that can address a wide variety of applications including solidification and microstructural evolution in materials processing (Boettinger et al. 2002; Chen 2002; Thornton et al. 2003; Moelans et al. 2008) and solid mechanics problems for failure (Amiri et al. 2014, 2016; Areias et al. 2016a, b, c).

The advantage of the PFM lies in the fact that the model was designed to circumvent the numerical problem of tracking a sharp solid–liquid interface. Its principal characteristic is the regularization of the sharp interface with a diffuse interface between two phases where the diffuse interface is described by a steep but continuous transition of the phase-field variable between two different states. The implications of the regularization in terms of the micro force balances and the discussion about the limit to the sharp interface can be found in Fried and Gurtin (1993) and Gurtin and Fried (1994, 1996). In the PFM, the order parameters are constant in the respective phase and vary only within the very narrow diffusive interface region. Furthermore, the distinct length scales are typically involved in the systems having complex branched structures such as dendritic solidification, electrochemical deposition, growth of bacterial colonies, etc. Resolving these intricate features requires a very fine spatial discretization but such a higher resolution is only required in the vicinity of the diffusive interface. Moreover, the PFM often needs to handle the second- and higher-order derivatives in the relevant governing equations. As a result, the PFM naturally demands the flexibility and adaptivity of the numerical scheme for the treatment of high order differential operators.

Conventional numerical techniques such as the finite difference method (FDM) and the finite element

method (FEM) have been widely used for the analysis of the PFM (Rosam et al. 2007; Du and Zhang 2008; Wise et al. 2007; Cenicerros et al. 2010; Lowengrub et al. 2009; Yue et al. 2006). An adaptive mesh refinement scheme based on these methods has been applied to various PFMs extending from pure materials solidification to binary alloy phase transformation and some biomechanical problems. In practical engineering applications, simple geometries are relatively rare. Numerical methods based on structured mesh have difficulties in capturing the intricate features of interface involved in high order governing equations. For example, the FEM has a merit of handling the second-order spatial operators. However, there are no such general and efficient numerical techniques for the moving interface problems with the higher-order differential operators. Consequently, special methods have been introduced to handle such issues.

An example of such a special method is the isogeometric analysis. An interesting application on solving the Cahn–Hilliard equation involving fourth-order spatial derivatives can be found in Gomez et al. (2008). It was reported that the method possesses a unique combined resolution of handling higher-order differential operators and three-dimensional geometric complexity. However, the mesh generation is still a major bottleneck to improve the efficiency of this approach. Adaptive mixed finite element approaches can deal with the high-order characteristics by reformulating the model as a system of second-order partial differential equations. However, this approach still induces high computational cost at a given accuracy (Du and Zhang 2006). Additional adaptive methods also include a Fourier spectral moving-mesh method (Zhu et al. 1999), and the finite volume approach (Lan and Chang 2003; Tan et al. 2007) for unstructured grids. Recently, Rosolen et al. (2013) and Peco et al. (2013) presented an adaptive meshfree method to model the shape deformation of biomembranes using the PFMs with the local maximum-entropy meshfree basis functions via a direct Ritz–Galerkin method. Another possible development of efficient adaptive algorithms might be Nitsche’s formulations based on  $C^0$ -elements (Kim et al. 2016) and B-splines (Jiang and Kim 2016). However, these methods require extra terms to weakly impose the boundary conditions or

continuity of derivatives, which inevitably leads to additional computation cost.

In this paper, we propose a strong form collocation method, called the PDM (Yoon and Song 2014a, b, c), as the solution method of the PFM. The method possesses several desirable features of the aforementioned methods to solve the PFM. The PDM has important attributes: (1) it can easily handle the high-order derivatives in the relevant governing equations; (2) it employs only a point-wise computation on the basis of a variable support radius suitable for partial refinement and dynamic adaptivity; (3) it naturally inherits all advantages of the conventional meshfree methods; (4) the distribution of the collocation points can be easily adapted to resolve the intricate features of solutions; (5) it does not require numerical integration as it does not involve a weak formulation; (6) the particle derivative approximation dramatically accelerates the computational speed for derivative computations; (7) it has been shown that it possesses robustness and accuracy for moving interface problems (Yoon and Song 2014a, b, c) compared to other conventional meshfree methods.

In the meshfree (point-wise) collocation method, the majority of current available approaches can be classified into two major categories depending on whether the formalism of the method requires the *actual* derivative of an approximation field. If the *actual* derivative of the moving least-square approximation (MLSA) scheme is required, the method can be categorized into the conventional meshfree method such as the element-free Galerkin method (Belytschko et al. 1994) and the reproducing kernel particle method (Liu et al. 1995). The idea of actually differentiating MLSA scheme was first introduced in the element-free Galerkin method (Belytschko et al. 1994) as a correction for the inconsistent differentiation of the MLSA scheme. The reproducing kernel particle method (Liu et al. 1995) was also developed to provide more elegant mathematical derivation that can correct the kernel approximation of the smoothed particle hydrodynamics (Monaghan 1992) by enforcing the reproducing property of the polynomials up to the necessary order of consistency. Although the origin of both methods is different, their discrete forms for the approximations of solutions are quite analogous. Most meshfree methods based on weak formulations have employed this approach for computing derivatives.

On the other hand, if the *actual* differentiation of the MLSA scheme is not explicitly required in the formalism, the method falls into the category of the non-conventional meshfree method which needs the approximation of the derivatives in addition to the approximation of a solution field. Such an alternate approach was initiated by Nayroles et al. (1992) where the polynomial basis was differentiated during the numerical computations. This approach was named the diffuse derivative approximation. Although the diffuse derivative approximation provided an insight into the fast derivative computation of the MLSA, the method was not sufficiently supported by a mathematical foundation. Moreover, accuracy deficiencies emerged and thus diminishing the merit of fast derivative computation since it was combined with the weak formulation, which essentially requires the exact differentiation of the involved functions. Furthermore, Krongauz and Belytschko (1997a, b) discussed the lack of integrability of the test function when the diffuse derivative was used within the context of the Petrov–Galerkin formulation. Also, Huerta et al. (2004) presented a pseudo divergence-free field for the diffuse derivative approximation in the framework of weak formulation for an incompressible fluid flow problem.

In addition, Li and Liu (1998, 1999, 2002) developed a hierarchical partition of unity of reproducing kernel function approach. This approach enabled the elegant proof of the mathematical fundamentals of the diffuse derivative approximation by the hierarchical partition of unity and a hierarchical basis. Kim and Kim (2003) also proved the reproducing property of the diffuse derivative approximation. They showed that the approximation can be derived from the construction of the Taylor series associated with the MLSA. Subsequently, Lee and Yoon (2004) showed that the diffuse derivative approximation mathematically consists of the sequential operations of the polynomial derivative and moving process without losing the reproducing property. More importantly, Kim and Kim (2003) and Lee and Yoon (2004) applied the diffuse derivative approximation in the strong formulation to solve fluid and solid mechanics problems since the reproducing property (or consistency) is necessary and sufficient condition for the strong formulation. The meshfree point collocation method combined with the diffuse derivative approximation has been applied to various problems such as the

singularity due to layered material interface (Kim et al. 2007a, b) and the asymptotic crack tip singularity in a linear elastic fracture (Yoon et al. 2006). Onate et al. (1996a, b, 2001) and Aluru (2000) proposed a collocation method with the MLSA with fixed kernel functions. In their methods, the approximation and derivatives of a solution field can be evaluated at collocation points only due to the fixity of the kernel function.

Recently, Yoon and Song (2014a, b, c) proposed the extended PDM for weak and strong discontinuity problems. Though the method is the extension of the methods developed by Li and Liu (1998, 1999, 2002) and Kim and Kim (2003) with the extrinsic enrichments for various interface problems, the name “PDM” was introduced to emphasize the fact that the method is based on the strong form with the point-wise particle derivative approximation. Initially, the extended PDM was focused on various stationary singularity modeling techniques (Yoon and Song 2014a, b), and then was further extended to moving boundary problems such as the melting interface (Yoon and Song 2014c). It should be noted that the method developed in the present study shares a very similar mathematical foundation with the PDM, but it is enhanced by several implementation details. In the present study, the PDM that combines the multi-phase field model (MPFM) and heat transfer analysis, is presented. Its reliability and accuracy in solving the coupled thermo-solidification problems are demonstrated.

The remainder of the paper is organized as follows. In Sect. 2, we present the MPFM describing the polycrystalline growth initiating from the undercooled melt material. In Sect. 3, the PDM for solving the MPFM is described in detail. In Sect. 4, computational details as well as the simulation results are presented for the coupled thermo-solidification problem. Finally, in Sect. 5, we provide conclusions and summary of directions for future work.

## 2 Coupled multi-phase field model with heat transfer

As indicated in the previous section the primary purpose of the present study is to apply the PDM to the simulation of microstructure evolution during solidification. This is to verify the computational feasibility

of the PDM to the diffusive interface approach such as the MPFM (Steinbach and Pezzolla 1999; Eiken et al. 2006; Steinbach 2009). The MPFM is a variant of the conventional PFM developed to address the evolution of an arbitrary number of different grains of the same phase that are distinct only by their orientations.

In the MPFM, each grain  $\alpha$  that is distinct from other grains either by its orientation or phase (or both) is associated with a unique phase-field variable, denoted by  $\phi_\alpha$ . The general free energy description in a domain  $\Omega$  may be formulated to account for multiple physical phenomena including contributions from the interfacial energy  $f^{\text{inf}}$ , the chemical energy  $f^{\text{chem}}$ , and the elastic energy  $f^{\text{elast}}$ . In this study, the elastic energy  $f^{\text{elast}}$  is assumed to have a null contribution and the chemical energy  $f^{\text{chem}}$  is considered for a pure material system. To represent the additive decomposition of each individual free energy contribution (Steinbach 2009), the total free energy functional  $F$  of a system can be written as

$$F = \int_{\Omega} (f^{\text{inf}} + f^{\text{chem}}) d\Omega \quad (2.1)$$

$$f^{\text{inf}} = \sum_{\alpha, \beta=0, \dots, N, \alpha \neq \beta} \frac{4\sigma_{\alpha\beta}}{\eta_{\alpha\beta}} \left\{ -\frac{\eta_{\alpha\beta}^2}{\pi^2} \nabla \phi_\alpha \cdot \nabla \phi_\beta + \phi_\alpha \phi_\beta \right\}, \quad (2.2)$$

$$f^{\text{chem}} = \sum_{\alpha=0, \dots, N} \phi_\alpha f_\alpha, \quad (2.3)$$

where  $f_\alpha$  is the bulk free energy of phase/grain  $\alpha$ . For the system consisting of  $N$  grains and the liquid phase,  $\phi_0$  represents the phase-field variable for the liquid phase and  $\phi_\alpha$ ,  $\alpha = 1, \dots, N$ , is the phase-field variable for grain  $\alpha$ . While  $\phi_\alpha = 1$  indicates the presence of phase/grain  $\alpha$ ,  $\phi_\alpha = 0$  represents the absence of grain  $\alpha$ . Here,  $\sigma_{\alpha\beta}$  is the interfacial energy between grains/phases  $\alpha$  and  $\beta$  and  $\eta_{\alpha\beta}$  is the interface width. Note that  $\eta_{\alpha\beta}$  is assumed to be constant  $\eta$  for all interfaces in this study, and the summation of all phase field variables at a spatial point  $\mathbf{x}$  and time instance  $t$  should be unity, i.e.,  $\sum_{\alpha=0}^N \phi_\alpha(\mathbf{x}, t) = 1$ .

The evolution of  $\phi_\alpha$  can be derived as

$$\frac{\partial \phi_\alpha}{\partial t} = - \sum_{\beta=1}^N \frac{\pi^2}{8m\eta} \mu_{\alpha\beta} \left( \frac{\delta F}{\delta \phi_\alpha} - \frac{\delta F}{\delta \phi_\beta} \right) \quad (2.4)$$

where  $\delta F / \delta \phi_\alpha$  is the variational derivative of the free

energy functional  $F$  with respect to the phase-field variable  $\phi_\alpha$ . From (2.4), we can obtain the thermodynamically consistent phase field evolution equation

$$\frac{\partial \phi_\alpha}{\partial t} = \sum_{\beta=1}^N \frac{\mu_{\alpha\beta}}{m} \left\{ \sum_{\gamma=1}^N (\sigma_{\beta\gamma} - \sigma_{\alpha\gamma}) I_\gamma + \frac{\pi^2}{8\eta} \Delta g_{\alpha\beta} \right\}, \quad (2.5)$$

$$I_\gamma = \nabla^2 \phi_\gamma + \frac{\pi^2}{\eta^2} \phi_\gamma \quad (2.6)$$

where  $\mu_{\alpha\beta}$  is the interfacial mobility at the boundary of phases/grains  $\alpha$  and  $\beta$  and  $\Delta g_{\alpha\beta}$  is the free energy difference between phases  $\alpha$  and  $\beta$ . Here,  $m$  represents the local number of existing grains (or phases) meeting at a grid point. Note that it indicates the existence of the grain  $\alpha$  at the grid point  $\mathbf{x}$  if  $\phi_\alpha(\mathbf{x}) > 0$  and  $m$  is usually less than 10 (Kim et al. 2006).

However, this thermodynamically consistent form disturbs the traveling wave solution of the double obstacle potential; for details, refer to Steinbach (2009). As a consequence, in most simulations, the so-called antisymmetric approximation is adopted at the multiple junctions when using the MPFM (Eiken et al. 2006):

$$\frac{\partial \phi_\alpha}{\partial t} = \sum_{\beta=1}^N \mu_{\alpha\beta} \left\{ \sigma_{\alpha\beta} \left( \phi_\beta \nabla^2 \phi_\alpha - \phi_\alpha \nabla^2 \phi_\beta \right) + \frac{\pi^2}{2\eta^2} (\phi_\alpha - \phi_\beta) \right\} + \frac{\pi}{\eta} \sqrt{\phi_\alpha \phi_\beta} \Delta g_{\alpha\beta}. \quad (2.7)$$

In particular, a weighting function is introduced to concentrate the thermodynamic driving force to the center of the interface, and the diffusive terms are weighted by the phase field variable of the counter phase. However, (2.7) cannot be rigorously derived from a free energy formulation and the energy balance may be violated at the triple junctions (Eiken et al. 2006; Steinbach et al. 1996).

The influence of the liquid–solid phase transition on the temperature field  $T(\mathbf{x}, t)$  is investigated by considering the heat transfer equation

$$\frac{\partial T}{\partial t} = \alpha \nabla^2 T + \frac{1}{c_p \rho} q \quad (2.8)$$

where  $\alpha = \kappa / \rho c_p$  is the thermal diffusivity with the heat conductivity  $\kappa$ , the density  $\rho$ , and the specific heat capacity  $c_p$ . The heat source  $q$  generated or absorbed

from the solid–liquid transformation can be represented by

$$q = -\rho L \frac{\partial \phi_0}{\partial t} \quad (2.9)$$

where  $L$  is the latent heat and  $\partial \phi_0 / \partial t$  represents the rate of the change of the liquid phase-field variable.

The solution procedure for this study is as follows. The phase-field evolution equation (2.7) is first solved to yield the liquid phase change and the heat source  $q$  from (2.9) is computed from the phase change obtained at the collocation point. Then, the variation of temperature is evaluated using the heat transfer equation (2.8). Notice that (2.7) and (2.8) are coupled with a conventional staggered explicit solution scheme.

### 3 Numerical methodology

#### 3.1 Particle difference method

The PDM (Yoon and Song 2014a, b, c) is based on the strong formulation derived by a Taylor series involving the point-wise derivative approximation. For convenience, we first introduce the relevant mathematical notation. Let  $\mathbf{x} = (x_1, \dots, x_n)$  be the  $n$ -dimensional real vector and  $\boldsymbol{\alpha} = (\alpha_1, \dots, \alpha_n)$  be the  $n$ -tuple of non-negative integers. The  $\boldsymbol{\alpha}$ -th power of  $\mathbf{x}$  is defined by

$$\mathbf{x}^{\boldsymbol{\alpha}} = x_1^{\alpha_1} x_2^{\alpha_2} \cdots x_n^{\alpha_n}. \quad (3.1)$$

We define the  $\boldsymbol{\alpha}$ -th derivative of a function  $f(\mathbf{x})$  with respect to  $\mathbf{x}$  as

$$D_{\mathbf{x}}^{\boldsymbol{\alpha}} f(\mathbf{x}) = \frac{\partial^{|\boldsymbol{\alpha}|} f(\mathbf{x})}{\partial x_1^{\alpha_1} \partial x_2^{\alpha_2} \cdots \partial x_n^{\alpha_n}}, \quad (3.2)$$

where  $|\boldsymbol{\alpha}|$  is the sum of all components of  $\boldsymbol{\alpha}$ , i.e.,  $|\boldsymbol{\alpha}| = \sum_{i=1}^n \alpha_i$ . The  $m$ -th order Taylor series polynomial approximating a continuous function  $u(\mathbf{x})$  at the local center  $\bar{\mathbf{x}}$  that neglects terms of order higher than  $m$ , can be expressed as

$$u(\mathbf{x}) = \sum_{|\boldsymbol{\alpha}| \leq m} \frac{(\mathbf{x} - \bar{\mathbf{x}})^{\boldsymbol{\alpha}}}{\boldsymbol{\alpha}!} D_{\mathbf{x}}^{\boldsymbol{\alpha}} u(\bar{\mathbf{x}}) = \mathbf{p}_m^{\top}(\mathbf{x}) \mathbf{a}(\bar{\mathbf{x}}), \quad (3.3)$$

where  $\boldsymbol{\alpha}!$  is the factorial of  $\boldsymbol{\alpha}$ , i.e.,  $\boldsymbol{\alpha}! = \alpha_1! \cdots \alpha_n!$ . Note that (3.3) can be decomposed into the polynomial

vector  $\mathbf{p}_m^\top(\mathbf{x})$  and the derivative coefficient vector  $\mathbf{a}(\bar{\mathbf{x}})$  computed at the local center. Thus, the polynomial vector can be expressed by the form

$$\mathbf{p}_m^\top(\mathbf{x}) = \left[ \frac{(\mathbf{x} - \bar{\mathbf{x}})^{\alpha_1}}{\alpha_1!}, \dots, \frac{(\mathbf{x} - \bar{\mathbf{x}})^{\alpha_L}}{\alpha_L!} \right], \quad (3.4)$$

where  $\alpha_i$  are the  $n$ -dimensional non-negative integer vectors and  $L = (n + m)! / (n!m!)$  is the number of the components of the polynomial vector  $\mathbf{p}_m^\top$ .  $\alpha_L = (0, \dots, m)$  and  $m$  denote the highest exponent expressed by multi-index and the order of consistency of the Taylor polynomial, respectively. Also,  $(\mathbf{x} - \bar{\mathbf{x}})^{\alpha_i}$  is easily defined by (3.1).

The derivative coefficient vector can be defined as

$$\mathbf{a}^\top(\bar{\mathbf{x}}) = [D_{\mathbf{x}}^{\alpha_1} u(\bar{\mathbf{x}}), \dots, D_{\mathbf{x}}^{\alpha_L} u(\bar{\mathbf{x}})], \quad (3.5)$$

which includes all of the derivatives for  $u(\bar{\mathbf{x}})$  at  $\bar{\mathbf{x}}$  up to the order of consistency or  $\alpha_L$ -th order.

For the construction of the approximated fields, the PDM also adopts the MLSA procedure based on point-wise computation. In fact, this procedure quite resembles that of the derivative approximation of the meshfree point collocation method (Kim and Kim 2003; Lee and Yoon 2004; Kim et al. 2007a, b; Yoon et al. 2006). To determine  $\mathbf{a}(\bar{\mathbf{x}})$ , we introduce the weighted discrete  $L^2$ -norm given by

$$J = \sum_{I=1}^N w \left( \frac{\mathbf{x}_I - \bar{\mathbf{x}}}{\rho_{\bar{\mathbf{x}}}} \right) [\mathbf{p}_m^\top(\mathbf{x}_I; \bar{\mathbf{x}}) \mathbf{a}(\bar{\mathbf{x}}) - u_I]^2, \quad (3.6)$$

where  $N$  is the number of collocation points included in the neighborhood of  $\bar{\mathbf{x}}$  for which the weight function  $w \neq 0$ , and  $u_I$  refer to the nodal solution of  $u(\mathbf{x})$  at the collocation point  $I$ . Here,  $\rho_{\bar{\mathbf{x}}}$  is the dilation function indicating the radius of the weight function and determines the size of the neighborhood of  $\bar{\mathbf{x}}$  (Kim and Kim 2004).

The minimization of  $J$  in (3.6) with respect to  $\mathbf{a}(\bar{\mathbf{x}})$ , i.e.,  $\partial J / \partial \mathbf{a} = 0$ , gives rise to the linear equation

$$\mathbf{M}(\bar{\mathbf{x}}) \mathbf{a}(\bar{\mathbf{x}}) = \mathbf{B}(\bar{\mathbf{x}}) \mathbf{u} \quad (3.7)$$

or the derivative coefficient vector

$$\mathbf{a}(\bar{\mathbf{x}}) = \mathbf{M}^{-1}(\bar{\mathbf{x}}) \mathbf{B}(\bar{\mathbf{x}}) \mathbf{u}, \quad (3.8)$$

where

$$\mathbf{M}(\bar{\mathbf{x}}) = \sum_{I=1}^N w \left( \frac{\mathbf{x}_I - \bar{\mathbf{x}}}{\rho_{\bar{\mathbf{x}}}} \right) \mathbf{p}_m(\mathbf{x}_I; \bar{\mathbf{x}}) \mathbf{p}_m^\top(\mathbf{x}_I; \bar{\mathbf{x}}), \quad (3.9)$$

$$\mathbf{B}(\bar{\mathbf{x}}) = \begin{bmatrix} w \left( \frac{\mathbf{x}_1 - \bar{\mathbf{x}}}{\rho_{\bar{\mathbf{x}}}} \right) \mathbf{p}_m(\mathbf{x}_1; \bar{\mathbf{x}}), \\ w \left( \frac{\mathbf{x}_2 - \bar{\mathbf{x}}}{\rho_{\bar{\mathbf{x}}}} \right) \mathbf{p}_m(\mathbf{x}_2; \bar{\mathbf{x}}), \dots, w \left( \frac{\mathbf{x}_N - \bar{\mathbf{x}}}{\rho_{\bar{\mathbf{x}}}} \right) \mathbf{p}_m(\mathbf{x}_N; \bar{\mathbf{x}}) \end{bmatrix}, \quad (3.10)$$

and

$$\mathbf{u}^\top = [u_1, u_2, \dots, u_N]. \quad (3.11)$$

Substituting  $\mathbf{x}$  for  $\bar{\mathbf{x}}$  in (3.8) and  $\alpha_i$ -th component of  $\mathbf{a}(\mathbf{x})$  yields a general form of the particle derivative approximation as

$$D_{\mathbf{x}}^{\alpha_i} u(\mathbf{x}) = \Phi^{\alpha_i}(\mathbf{x}) \mathbf{u}, \quad (3.12)$$

for  $0 < |\alpha_i| \leq m$ . The shape function matrix  $\Phi^{\alpha_i}(\mathbf{x})$  represents a collection of  $\alpha_i$ -th derivative approximations of nodal shape functions and can be expressed as

$$\Phi^{\alpha_i}(\mathbf{x}) = \mathbf{e}_{\alpha_i}^\top \mathbf{M}^{-1}(\mathbf{x}) \mathbf{B}(\mathbf{x}). \quad (3.13)$$

Namely,  $\Phi^{\alpha_i}(\mathbf{x}) = [\Phi_1^{\alpha_i}(\mathbf{x}), \dots, \Phi_N^{\alpha_i}(\mathbf{x})]$ . Also,  $\mathbf{e}_{\alpha_i}^\top = (0, \dots, 1, \dots, 0)$ , in which 1 is placed at the  $\alpha_i$ -th slot of  $\mathbf{e}_{\alpha_i}^\top$  in lexicographic order. In a matrix form, (3.12) can be rewritten as

$$\begin{pmatrix} D_{\mathbf{x}}^{\alpha_1} u(\mathbf{x}) \\ D_{\mathbf{x}}^{\alpha_2} u(\mathbf{x}) \\ \vdots \\ D_{\mathbf{x}}^{\alpha_L} u(\mathbf{x}) \end{pmatrix} = \begin{bmatrix} \Phi_1^{\alpha_1}(\mathbf{x}) & \Phi_2^{\alpha_1}(\mathbf{x}) & \cdots & \Phi_N^{\alpha_1}(\mathbf{x}) \\ \Phi_1^{\alpha_2}(\mathbf{x}) & \Phi_2^{\alpha_2}(\mathbf{x}) & \cdots & \Phi_N^{\alpha_2}(\mathbf{x}) \\ \vdots & \vdots & \ddots & \vdots \\ \Phi_1^{\alpha_L}(\mathbf{x}) & \Phi_2^{\alpha_L}(\mathbf{x}) & \cdots & \Phi_N^{\alpha_L}(\mathbf{x}) \end{bmatrix} \begin{pmatrix} u_1 \\ u_2 \\ \vdots \\ u_N \end{pmatrix}, \quad (3.14)$$

where  $\alpha_i$  represent 3-tuples of non-negative integers, e.g.,  $\alpha_1 = (0, 0, 0)$ ,  $\alpha_2 = (1, 0, 0)$ ,  $\alpha_3 = (0, 1, 0)$ ,  $\dots$ ,  $\alpha_L = (0, 0, m)$ .

From (3.12), the approximation  $u^h(\mathbf{x})$  of the solution field  $u(\mathbf{x})$  can be represented by

$$u^h(\mathbf{x}) := D_{\mathbf{x}}^0 u(\mathbf{x}) = \Phi^{(0,0,0)}(\mathbf{x}) \mathbf{u}. \quad (3.15)$$

Since  $\Phi^{\alpha_i}(\mathbf{x})$  is composed with the  $\alpha_i$ -th derivative approximations of the nodal shape functions, the particle derivative approximation can be written more specifically in the form

$$D_{\mathbf{x}}^{\alpha_i} u(\mathbf{x}) = \sum_{I=1}^N \Phi_I^{\alpha_i}(\mathbf{x}) u_I. \quad (3.16)$$

In this study, (2.7) and (2.8) involve the second-order derivatives of field variables. Thus, we employ the second-order polynomial vector with  $m = 2$  in (3.4).



For  $m = 2$ , the composition of the derivative coefficient vector is given by

$$\begin{pmatrix} D_{\mathbf{x}}^{(0,0,0)} u(\mathbf{x}) \\ D_{\mathbf{x}}^{(1,0,0)} u(\mathbf{x}) \\ \vdots \\ D_{\mathbf{x}}^{(0,1,1)} u(\mathbf{x}) \\ D_{\mathbf{x}}^{(0,0,2)} u(\mathbf{x}) \end{pmatrix} = \left[ u(\mathbf{x}), \frac{\partial u(\mathbf{x})}{\partial x_1}, \dots, \frac{\partial u^2(\mathbf{x})}{\partial x_2 \partial x_3}, \frac{\partial u^2(\mathbf{x})}{\partial x_3^2} \right]^T. \quad (3.17)$$

The matrices  $\mathbf{M}(\mathbf{x})$  and  $\mathbf{B}(\mathbf{x})$  can then be computed as

$$\mathbf{M}(\mathbf{x}) = \sum_{l=1}^N w\left(\frac{\mathbf{x}_l - \mathbf{x}}{\rho_{\mathbf{x}}}\right) \mathbf{p}_2(\mathbf{x}_l; \mathbf{x}) \mathbf{p}_2^T(\mathbf{x}_l; \mathbf{x}), \quad (3.18)$$

$$\mathbf{B}(\mathbf{x}) = w\left(\frac{\mathbf{x}_1 - \mathbf{x}}{\rho_{\mathbf{x}}}\right) \mathbf{p}_2(\mathbf{x}_1; \mathbf{x}), \dots, w\left(\frac{\mathbf{x}_N - \mathbf{x}}{\rho_{\mathbf{x}}}\right) \mathbf{p}_2(\mathbf{x}_N; \mathbf{x}). \quad (3.19)$$

The PDM uses the weight function  $w\left(\frac{\mathbf{x}_l - \mathbf{x}}{\rho_{\mathbf{x}}}\right)$  with a non-zero compact support over a neighborhood of  $\mathbf{x}$  that generates a linear equation for the derivative approximation. In contrast to conventional meshless methods, the PDM can use any function with a conical shape as a weight function because no differentiability for the weight function is required in the PDM formulation. As long as the function is non-negative and continuous, the smoothness is not necessary. On the other hand, other meshless methods demand the differentiability of the weight function because the derivative of the approximation includes the derivative of the weight function (Yoon and Song 2014a; Kim and Kim 2003; Lee and Yoon 2004). In the present we employ non-differentiable functions with sharp peaks and discontinuous derivatives as follows:

$$w_1\left(\frac{x-y}{\rho_y}\right) = \left(1 - \left\|\frac{x-y}{\rho_y}\right\|\right)^4 \quad (3.20)$$

$$w_2\left(\frac{x-y}{\rho_y}\right) = \left(1 - \left\|\frac{x-y}{\rho_y}\right\|^{1/2}\right)^2. \quad (3.21)$$

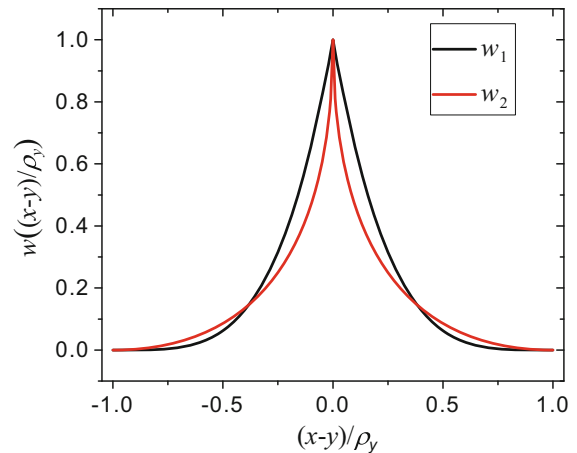


**Fig. 1** Examples of non-smooth weight functions

It should be noted that non-smooth weight functions have also been used previously (Kim and Kim 2003; Lee and Yoon 2004) in the framework of the meshfree point collocation method. Figure 1 illustrates an example of non-smooth weight functions as given by (3.20) and (3.21).

Conventional weak form based meshfree methods have used smooth (i.e., continuously differentiable) weight functions because they require the exact derivative of the approximation function for ensuring integrability. In contrast, it was recognized that for the PDM which is based on the strong form, the non-smooth functions exhibit better performance than the smooth ones due to their resemblance to the Dirac delta function (Yoon and Song 2014a, b).

### 3.2 Spatial and temporal discretizations

In the PDM, (2.7) and (2.8) are directly discretized based on the point-wise particle difference scheme. This involves discretization of the computational domain by distributing collocation points in the interior domain and on the boundaries. As seen in the previous section, the PDM provides the particle derivative approximation up to the order of consistency. The particle derivative approximation may not be termed as an interpolant because it does not use a predefined interpolant such as a standard finite-element shape function. It is rather constructed at the position of interest when necessary. Applying the forward Euler scheme to (2.7) and (2.8) yields

$$\frac{\phi_\alpha^{n+1} - \phi_\alpha^n}{\Delta t} = \sum_{\beta=1}^N \mu_{\alpha\beta} \left\{ \sigma_{\alpha\beta} \left( \phi_\beta^n \nabla_h^2 \phi_\alpha^n - \phi_\alpha^n \nabla_h^2 \phi_\beta^n \right) + \frac{\pi^2}{2\eta^2} (\phi_\alpha^n - \phi_\beta^n) \right\} + \frac{\pi}{\eta} \sqrt{\phi_\alpha^n \phi_\beta^n} \Delta g_{\alpha\beta}, \quad (3.22)$$

$$\frac{T^{n+1} - T^n}{\Delta t} = \alpha \nabla_h^2 T^n + \frac{1}{c_p \rho} q^n, \quad (3.23)$$

where  $\Delta t$  is the timestep and the superscript on the phase field  $\phi$  and the temperature field  $T$  represents the index for the timestep. The operator  $\nabla_h^2$  denotes a discrete form of the Laplacian operator. As seen in (2.9),  $q^n$  includes the time-dependent term for the liquid phase field variable such that time integration will be conducted on this term.

In the present study, the coupled multi-phase field and heat transfer problem expressed by (2.7) and (2.8) is solved in a consecutive manner. Note that the multi-phase field equation (2.7) and the heat transfer equation (2.8) utilize the periodic boundary condition and therefore additional treatment for the boundary condition is not necessary. During the simulation, all the collocation points in the numerical model are technically treated as interior collocation points and the computation process becomes quite straightforward.

In the PDM framework, (3.22) yields the system of equations

$$\mathbf{L} \cdot \boldsymbol{\phi}_\alpha^{n+1} = \mathbf{F}^\phi. \quad (3.24)$$

where

$$\mathbf{L} = \begin{bmatrix} L_1(\mathbf{x}_1) & \cdots & L_N(\mathbf{x}_1) \\ \vdots & \ddots & \vdots \\ L_1(\mathbf{x}_N) & \cdots & L_N(\mathbf{x}_N) \end{bmatrix}, \quad (3.25)$$

$$\boldsymbol{\phi}_\alpha^{n+1} = \begin{pmatrix} \phi_{\alpha 1}^{n+1} \\ \vdots \\ \phi_{\alpha N}^{n+1} \end{pmatrix}, \quad (3.26)$$

$$\mathbf{F}^\phi = \begin{pmatrix} F^\phi(\mathbf{x}_1) \\ \vdots \\ F^\phi(\mathbf{x}_N) \end{pmatrix}, \quad (3.27)$$

with the subscript  $I$  being the nodal index and the superscript  $n+1$  being the timestep. Thus, it can be noticed that the  $J$ -th equation of the system in (3.24) can be obtained by assembling the following discrete equations

$$\sum_{I=1}^N L_I(\mathbf{x}_J) \phi_{\alpha I}^{n+1} = F^\phi(\mathbf{x}_J). \quad (3.28)$$

Here, the discrete differential operator  $L_I(\mathbf{x}_J)$  is given by

$$L_I(\mathbf{x}_J) = \Phi_I^{(0,0,0)}(\mathbf{x}_J), \quad (3.29)$$

and the generalized force  $F^\phi(\mathbf{x}_J)$  takes the form

$$\begin{aligned} F_\phi^\Omega(\mathbf{x}_J) = & \sum_{I=1}^N \Phi_I^{(0,0,0)}(\mathbf{x}_J) \phi_{\alpha I}^n \\ & + \Delta t \sum_{\beta=1}^N \mu_{\alpha\beta} \left\{ \sigma_{\alpha\beta} \left[ \left( \sum_{I=1}^N \Phi_I^{(0,0,0)}(\mathbf{x}_J) \phi_{\beta I}^n \right) \right. \right. \\ & \times \sum_{I=1}^N \left( \Phi_I^{(2,0,0)}(\mathbf{x}_J) + \Phi_I^{(0,2,0)}(\mathbf{x}_J) + \Phi_I^{(0,0,2)}(\mathbf{x}_J) \right) \phi_{\alpha I}^n \\ & - \left( \sum_{I=1}^N \Phi_I^{(0,0,0)}(\mathbf{x}_J) \phi_{\alpha I}^n \right) \sum_{I=1}^N \left( \Phi_I^{(2,0,0)}(\mathbf{x}_J) + \Phi_I^{(0,2,0)}(\mathbf{x}_J) \right. \\ & \left. \left. + \Phi_I^{(0,0,2)}(\mathbf{x}_J) \right) \phi_{\beta I}^n + \frac{\pi^2}{2\eta^2} \sum_{I=1}^N \Phi_I^{(0,0,0)}(\mathbf{x}_J) (\phi_{\alpha I}^n - \phi_{\beta I}^n) \right] \\ & \left. + \frac{\pi}{\eta} \sqrt{\left( \sum_{I=1}^N \Phi_I^{(0,0,0)}(\mathbf{x}_J) \phi_{\alpha I}^n \right) \left( \sum_{I=1}^N \Phi_I^{(0,0,0)}(\mathbf{x}_J) \phi_{\beta I}^n \right) \Delta g_{\alpha\beta}} \right\}. \end{aligned} \quad (3.30)$$

Similarly, (3.23) yields the system of equations

$$\mathbf{L} \cdot \mathbf{T}^{n+1} = \mathbf{F}^T. \quad (3.31)$$

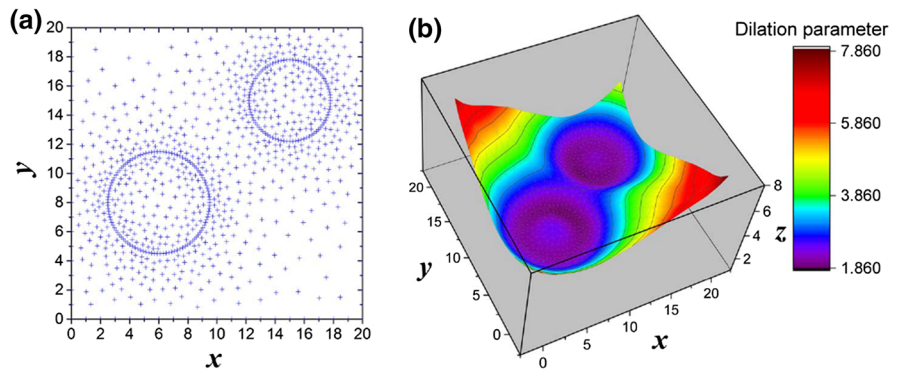
It can be recognized that (3.24) and (3.31) have a similar form. The only difference is that the vector of the unknowns and the generalized force vector are different according to the type of the particular unknown, i.e., the phase-field variable or temperature. The the  $J$ -th row of the system in (3.31) is constructed by assembling the following discrete form

$$\sum_{I=1}^N L_I(\mathbf{x}_J) T_I^{n+1} = F^T(\mathbf{x}_J) \quad (3.32)$$

where the discrete operator  $L_I(\mathbf{x}_J)$  is the same



**Fig. 2** Examples of **a** non-uniformly distributed collocation points and **b** the corresponding dilation function



with (3.29) and the generalized force term  $F^T(\mathbf{x}_J)$  can be computed as

$$\begin{aligned}
 F^T(\mathbf{x}_J) = & \sum_{l=1}^N \Phi_l^{(0,0,0)}(\mathbf{x}_J) T_l^n \\
 & + \alpha \Delta t \sum_{l=1}^N \left( \Phi_l^{(2,0,0)}(\mathbf{x}_J) + \Phi_l^{(0,2,0)}(\mathbf{x}_J) \right. \\
 & \left. + \Phi_l^{(0,0,2)}(\mathbf{x}_J) \right) T_l^n + \frac{\Delta t}{c_p \rho} q^n(\mathbf{x}_J).
 \end{aligned} \quad (3.33)$$

Here,  $q^n$  contains the time-dependent phase-field variable according to (2.9). Since the phase-field variable was already computed by solving (3.24),  $q^n$  can be discretized by

$$\begin{aligned}
 q^n(\mathbf{x}_J) \\
 = -\frac{\rho L}{\Delta t} \left( \sum_{l=1}^N \Phi_l^{(0,0,0)}(\mathbf{x}_J) \phi_{0l}^n - \sum_{l=1}^N \Phi_l^{(0,0,0)}(\mathbf{x}_J) \phi_{0l}^{n-1} \right),
 \end{aligned} \quad (3.34)$$

where  $\frac{\partial \phi_0}{\partial t}$  of (2.9) is differentiated in an explicit manner.

### 3.3 Computation of the shape function matrix and its parallelization

The support radius of the weight function  $\rho_x$  is associated with the moving least-square approximation and designates the size of the influence domain within which the Taylor polynomial in (3.3) is expanded; note that we used the variable support radius proposed by Kim and Kim (2004) for the computation of  $\rho_x$ . We construct a list containing all collocation points that are included in the domain of

support of each collocation point. With the variable support radius approach, the number of collocation points involved in the Taylor polynomial falls into the proper range regardless of the density or the local center of the collocation point, and unlike the Isogeometric collocation method (Anitescu et al. 2015), the PDM does not require additional collocation points to ensure its numerical stability. In other words, the variable dilation function  $\rho_x$  is employed such that the desirable number of neighbor collocation points that can ensure the numerical stability and accuracy are included within the domain of influence (or compact support) of the collocation point. As stated in Yoon and Song (2014a), the upper bound for the number of neighbor collocation points is associated with the computational efficiency and the lower bound is related to the invertibility of the moment matrix. At the same time, maintaining a proper size of support radius might affect the resolution of the particle derivative approximation in the presence of the density variation of the collocation points. In the present study, the support radius size is selected to be large enough to ensure the invertibility of the moment matrix.

Figure 2a shows an example of an irregular distribution of the collocation points in which the collocation points tend to be concentrated around the edges of two circles, i.e., inclusions, where higher spatial resolution is necessary for accurate modeling. The plot of  $\rho_x$  for this arrangement is presented in Fig. 2b. It demonstrates that  $\rho_x$  varies with respect to the position and the density of the collocation points. It becomes smaller at the edge of the circles to account for the high collocation density, while it is larger at the corner of the square domain where the collocation density is lower.

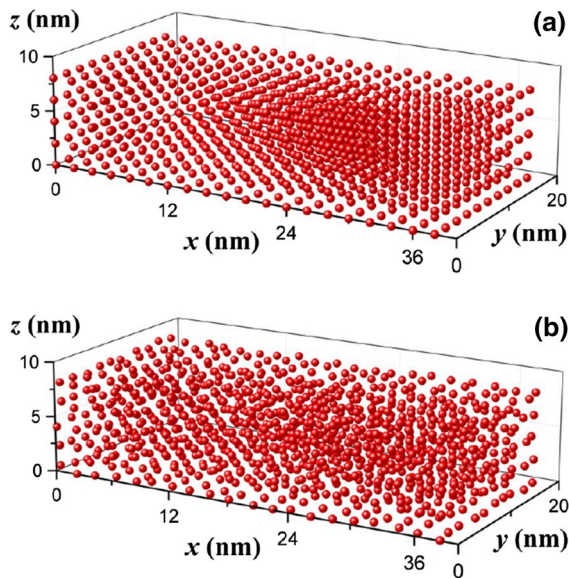


**Fig. 3** Examples of **a** a uniform and **b** a random distributions of the collocation points

The parallelization of the PDM (Fu et al. 2017) is realized in terms of the MPI parallelization technique at both off-line (i.e., computing the shape function matrix at collocation points) and on-line stages (i.e., assembling and solving discretized system of equations) by utilization of the PETSc library (Balay et al. 2016a, b). The main purpose to separate the computation into the off-line and on-line stages is to save the computational cost at the on-line stage by pre-computing the information that remains unchanged during the computation with a given set of initially distributed collocation points at the off-line stage. In contrast to other meshless methods, the PDM needs to compute the shape function matrix  $\Phi_I^z(\mathbf{x})$  only once at the off-line stage, if the spatial positions of the collocation points remain unchanged in local (or entire) region during the computational analysis. Note that if the pre-computed shape function matrix  $\Phi_I^z(\mathbf{x})$  is stored into the memory, it requires certain amount of additional memory usage. However, it is not excessive since the  $\Phi_I^z(\mathbf{x})$  matrix is in the form of a sparse matrix.

In this study, the coupled thermo-solidification problem does not provoke any geometric changes in the PDM framework. Thus, the relationship between the collocation points and their neighbors within the computational domain is not changed. As a result, the same shape function matrix  $\Phi_I^z(\mathbf{x})$  is used at the on-

line stage whenever it is required in assembling  $\mathbf{L}$  and  $\mathbf{F}$  in (3.24) and (3.31). Moreover, the influence of initial conditions and materials parameters can be investigated at the on-line stage without repeating the costly computation procedure, such as the construction of the list of neighboring points and the shape function matrix. In fact, these can be computed once in advance and be used by calling them from the preprocessing storage whenever necessary. In the case of uniformly distributed collocation points with a periodic boundary condition, the shape function matrix can even be computed only at a single collocation point because it is identical for all the collocation points. This is conducted by a subsequent proper row assignment of the shape function matrix of this single collocation point to the neighboring points of the remaining.

## 4 Numerical examples

### 4.1 Solidification of polycrystalline Nickel

The solidification of polycrystalline nickel (Ni) from undercooled melt is selected as an example to demonstrate the robustness and flexibility of the PDM applied to the diffusive interface approach, i.e., the MPFM. The materials parameters required for the MPFM include the interfacial mobility  $\mu$ , the interfacial energy  $\sigma$ , the free energy difference between solid and liquid phases  $\Delta g$ , the interface width  $\eta$ , and the melting temperature  $T_M$ . The heat equation requires the density  $\rho$ , the heat conductivity  $\kappa$ , the specific heat capacity  $c_p$ , and the latent heat  $L$ . Since the Ni system has been well investigated, the values of material parameters are available in the literature and listed in Table 1. The weak anisotropy in the interfacial free energy and the mobility is ignored in the current study.

The computational domain was selected to have dimensions of  $40 \text{ nm} \times 20 \text{ nm} \times 10 \text{ nm}$  in the  $x$ -,  $y$ -, and  $z$ -directions, respectively. Numerical analyses were performed for both uniformly and randomly distributed collocation points. For the case of uniformly distributed collocation points, we selected a collocation spacing of  $\Delta x = \Delta y = \Delta z = 2 \text{ \AA}$  in all three directions, thus ensuring a satisfactory resolution of the interface width  $\eta = 12 \text{ \AA}$ . This led to a total

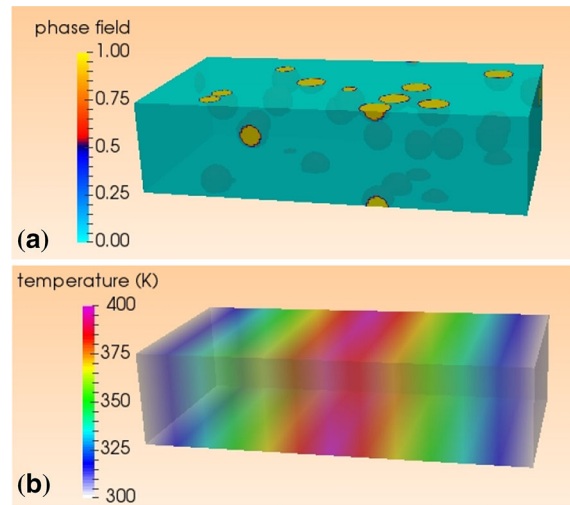
**Table 1** Materials parameters of a polycrystalline Ni

$\mu$	$2.56\text{E}-7 \text{ m}^2\text{s/kg}$	$\sigma$	$0.326 \text{ J/m}^2$
$\eta$	$12 \text{ \AA}$	$L$	$2.311\text{E}9 \text{ J/m}^3$
$T_M$	$1710 \text{ K}$	$\Delta g$	$\Delta g = L(T - T_M)/T_M$
$\kappa$	$80 \text{ W/(m K)}$	$c_p$	$440 \text{ J/(kgK)}$
$\rho$	$8.91\text{E}3 \text{ kg/m}^3$	$\alpha$	$2.06\text{E}-5 \text{ m}^2/\text{s}$

1,000,000 collocation points. For the case of randomly distributed collocation points, we maintained the same total number of points as with the case of the uniformly distributed collocation points. The nearest neighboring distance (i.e., collocation spacing) 1.8–2.2 Å is considered in this case. Examples of the uniformly and randomly distributed collocation points at a coarse level are displayed in Fig. 3a, b, respectively.

Unless otherwise specified, we chose the timestep  $\Delta t$  based on the Courant–Friedrichs–Lewy (CFL) condition. Using the materials parameters in Table 1, we obtain  $\Delta t \leq \Delta x^2/(6\mu\sigma) \approx 80 \text{ fs}$  for the MPFM and  $\Delta t \leq \Delta x^2/(6\alpha) \approx 0.26 \text{ fs}$  for the heat transfer problem. Notice that for the case of random distributions, the minimum value of  $\Delta x$  is typically used for the computation of the CFL condition due to the variation of  $\Delta x$ . However, it is worth mentioning that our numerical experiments indicated that the choice of a timestep in the range  $\Delta t = 0.1 \sim 1.0 \text{ fs}$  also ensures the numerical stability of both the MPFM and heat transfer models. In particular, choosing the time step for the time integration of the energy balance equation was thoroughly investigated with the PDM; some useful discussions on achieving the numerical stability in transient analysis for the parabolic PDE can be found in Yoon and Song (2014c).

Periodic boundary conditions are applied to all directions. The initial phase-field consisting of 20 grains of diameter around 3 nm is generated by randomly choosing their spherical centers as shown in panel (a) of Fig. 4. The liquid phase is associated with  $\phi_0$ , and the initially generated grains are assigned with  $\phi_1, \dots, \phi_{20}$ , where  $\phi_\alpha(\mathbf{x}) = 1$  if  $\mathbf{x}$  resides within the phase/grain  $\alpha$  and  $\phi_\alpha(\mathbf{x}) = 0$  otherwise. The initial temperature is taken to be a nonuniform distribution varying from 300 to 400 K along the  $x$ -direction to render a large undercooling degree as shown in Fig. 4b.

**Fig. 4** Initial **a** phase field and **b** temperature field of the Ni solidification problem

In this example, the solidification process of a polycrystalline Ni along with the temperature field is computed for three distinct cases; FDM and PDM on uniformly distributed nodes and PDM on randomly distributed collocation points. In Fig. 5, we show the results from the PDM with the uniform distribution of the collocation points as time evolves. Due to the high undercooling degree (i.e., the large difference between initial temperature and melting temperature), the material rapidly reaches a high level equilibrated state of solidification within a short time of 2 ps. The latent heat generated during the solidification process causes the presence of high temperature along the grain growth path, in the shape of an annulus as it can be observed from the temperature plots. Although the temperature at most collocation points appears to be well below the melting temperature (1710 K), there are few collocation points (fewer than 0.5%) that exhibit peak values over the melting point. Note that, in Figs. 5 and 7, the colorbar is adjusted mainly to accommodate the few overheated collocation points from the adiabatic condition adopted in the simulation and heat generated from the liquid–solid transformation. The spikes over the melting points can be observed for both the FDM and PDM approaches. This seemingly unphysical behavior was checked by increasing resolution up to two times for both uniform and random distributions and by reducing the timestep size by one-fifth. It was established that this is not sensitive to the specific temporal and spatial

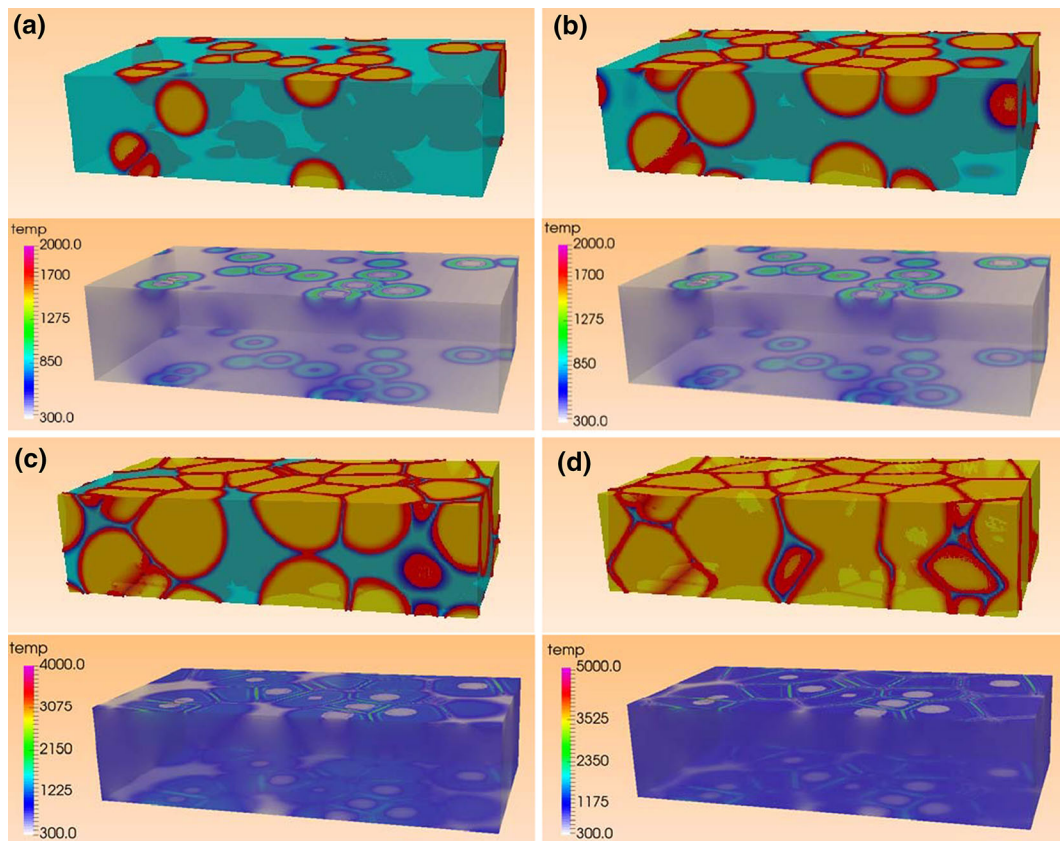


**Fig. 5** Evolution of phase and temperature fields obtained by the PDM at **a**  $4000\Delta t$ , **b**  $8000\Delta t$ , **c**  $12,000\Delta t$ , and **d**  $20,000\Delta t$  (The red isosurface represents  $\phi = 0.5$  in a solid phase)

discretization. However, this may be attributed to the phase field model itself and will remain as an important item of our future work for further investigation.

Figures 6 and 7 show the comparisons of the microstructural evolutions and temperature profiles for two arbitrarily selected timesteps for all three approaches. These three results are almost indistinguishable for both phase and temperature fields. This indicates the robustness of the developed method for both uniformly and randomly distributed collocation points. Although the parametric study results for various sizes of support radii are not presented here, we have established that a consistent accuracy can be obtained by employing the variable support radius  $\rho_x$ . In fact, the size of support radius may affect the resolution of numerical solution; as the size of support radius increases, discrepancy between the FDM and the PDM results may become larger. In other words, as the size of support radius decreases, the PDM result

becomes similar to the FDM result as long as the moment matrix is invertible. This emanates from the fact that the PDM generally uses the weight function with a pointed peak. When applying the small size of support radius, the relatively closer neighbor collocation points to the local center gives more contribution to the derivative approximation constitution than the further neighbor collocation points. So, careful selection of the weight and dilation functions is necessary.

In Table 2, the computational efficiency of the PDM approach is compared with the FDM for the case of the uniformly distributed collocation points, for which the same space decomposition algorithm for parallelization is utilized through PETSc. For the specific demonstration problem, the computational time for the FDM during the on-line stage was 5585.62 s with 25 processors and 3047.15 s with 50 processors. In contrast, the PDM requires 8214.29 and 4384.38 s computational time with 25 and 50 processors, respectively. It is worth mentioning that the



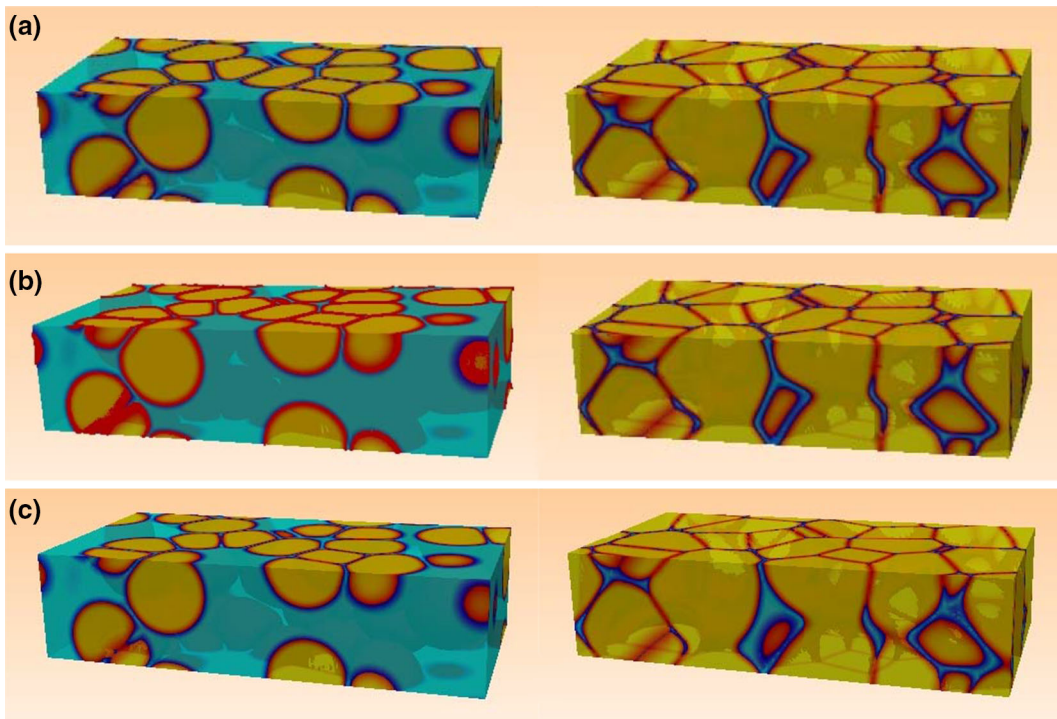


**Fig. 6** Comparisons among the phase fields obtained by **a** the FDM with a uniform node distribution, **b** the PDM with a uniform node distribution, and **c** the PDM with a random

distribution at  $8000\Delta t$  (left column) and  $16,000\Delta t$  (right column) (the red isosurface represents  $\phi = 0.5$  in a solid phase)

timestep adopted in the PDM is five times larger than the timestep of  $0.2 \text{ fs}$  in the FDM owing to the improved numerical stability; thus, fewer number of timesteps are required to reach the same time.

It is apparent that the PDM is more computationally demanding at each time step when compared with the FDM. This can be attributed to the fact that the FDM involves 7 grid points, while the PDM uses more neighbor collocation points (i.e., approximately 30 collocation points) to ensure the invertibility of the moment matrix. However, this issue can be addressed by the increasing the timestep size, and therefore, the difference between two approaches becomes not significant.

## 4.2 Scalability

The scalability of the parallelized code is tested by measuring its efficiency with increasing the number of parallel processors. The computing platform is the University of Colorado Boulder's mainframe cluster machine, JANUS, which is the 184-TFLOP (Trillion Floating Point Operations) supercomputer with 16,416

total cores. Each node contains two hex-core 2.8 GHz Intel Xeon Westmere processors for a total of 12 cores per node. The computational time at the off-line and on-line stages, as well as the speedup which is leading metric in measuring scaling, are calculated and recorded. Speedup is defined as the sequential program's running time on one core divided by the parallel program's running time on  $N$  processors (Kaminsky 2015), i.e.,

$$\text{Speedup}(N) = \frac{t_1}{t_N}, \quad (4.1)$$

where  $t_1$  represents the time to complete a work unit with one processing element and  $t_N$  is the amount of time to complete the same unit of work with  $N$  processing elements.

In the case of the strong scaling test, the number of processing elements is increased while the problem size stays fixed. Ideally, the speedup should be equal to the number of processors  $N$ . If the parallel program takes more time than the ideal, the speedup will be less than  $N$ . In addition, efficiency is a metric that tells how

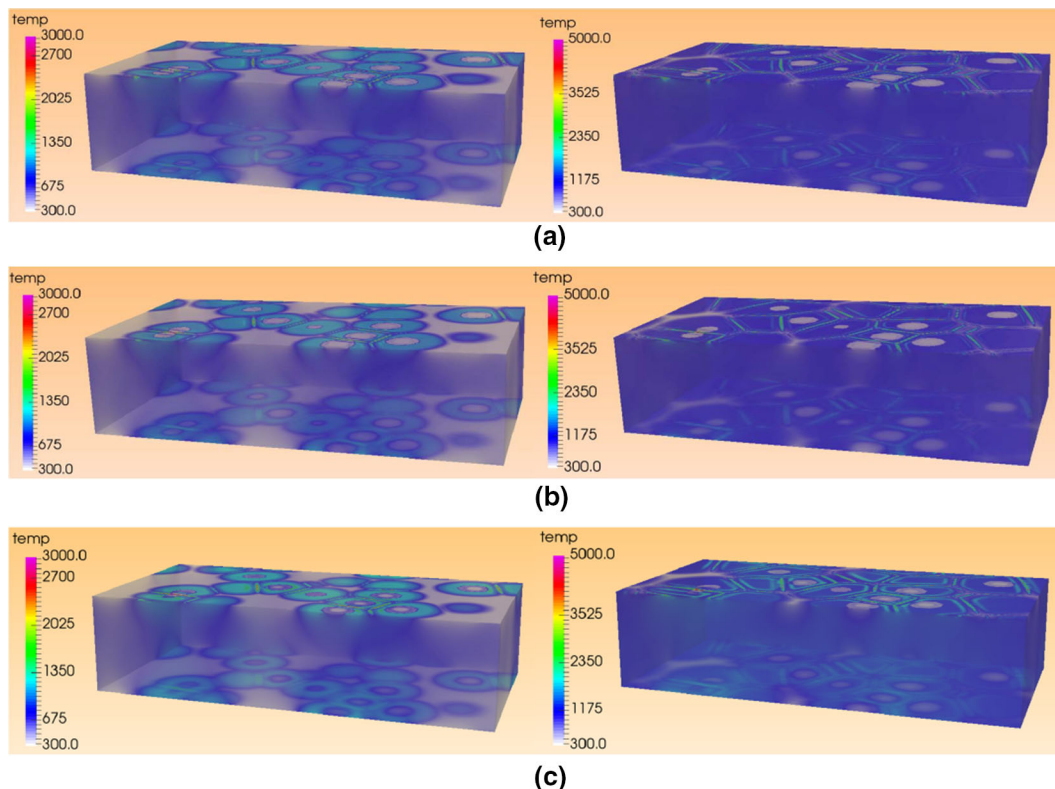


**Fig. 7** Comparisons among the temperature fields obtained by **a** the FDM with a uniform node distribution, **b** the PDM with a uniform distribution, and **c** the PDM with a random distribution

at  $8000\Delta t$  (left column) and  $16,000\Delta t$  (right column) (The red isosurface represents  $\phi = 0.5$  in a solid phase)

close to the ideal speedup giving the following expression:

$$E_{ff}(N) = \frac{\text{Speedup}(N)}{N} \times 100\%. \quad (4.2)$$

In general, it is hard to achieve a good strong-scaling efficiency since the communication overhead for most algorithms increases in proportion to the number of processors used.

The computational time and scalability efficiency at the off-line shape function matrix computation and the on-line equation solving stage of the example in Sect. 4.1 (totally 400 timesteps are computed at the on-line stage) are shown in Fig. 8. At the off-line stage, 50 processing elements (processors) are chosen as the reference (i.e.,  $E_{ff} = 100\%$ ) since prohibitively long computational time is required if one processor is used. Interestingly, with increasing number of processors, the scalability efficiency first increases until reaching a highest point at 250 processors when the nodal number is around 4000 per processor. In

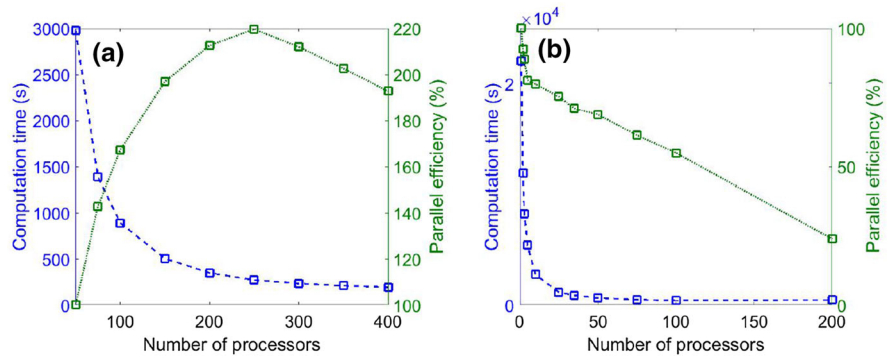
**Table 2** Comparison between the computational efficiency of FDM and PDM

Number of processors	FDM (s)	PDM (s)
25	5585.62	8214.29
50	3047.15	4384.38

contrast, the parallel efficiency at the on-line stage continuously decreases with increasing number of processors, especially when the processor number is below ten. It is therefore apparent that the communication overhead at the off-line stage is responsible for the continual decrease of parallel efficiency. A close examination of the numerical procedures at the off-line stage reveals very little communication overhead and is approximately subjected to a speedup of  $N$ . Thus we suspect the peculiar greater-than- $N$  speedup may be caused by the reduced memory allocation on each processor at the initial increase of



**Fig. 8** Computation time and parallel efficiency at the **a** off-line stage and **b** on-line stage



processor number, which affects the computation speed significantly.

#### 4.3 Sensitivity at the discretization level

To test the dependence of the PDM on the level of discretization, ten solid crystals are initially created in the cubic simulation domain with a size of  $1000 \text{ nm}^3$ . Periodic boundary conditions are applied to all directions, and the materials parameters are the same as those described above. The temperature is set as constant 300 K throughout the simulation, far below the melting temperature (1710 K). Consequently, the solid crystals begin to grow until a complete solidification in the simulation domain is achieved. We take three levels of spatial discretizations and the number of collocation points to discretize the spatial domain varies from 31,250 to 500,000.

Figure 9 shows the microstructural evolution at two time snapshots for three discretization levels. The grain structure similarity is apparent for all three discretization cases despite of the large variation among the respective total numbers of the collocation points. The only apparent discrepancy is the quality of the grain boundaries or the solid–liquid interfaces. Specifically, the image with 500,000 collocation points has sharp interfaces or grain boundaries while lower levels of discretizations become blurred and diffused. This could be partly attributed to the post-simulation image process stage as the smaller number of collocation points and interpolation values are available for the image generation. Therefore, the dependence on discretization on the PDM appears to be quite low.

Figure 10 shows the convergence of phase-field variable to a maximum value, as a function of the

number of collocation points. The convergence plateau value is calculated at a collocation point with the spatial coordinate  $(\Delta x, 26\Delta y, 6\Delta z)$  and is displayed at the time of  $1000\Delta t$ . It can be observed that the phase-field variable computed by the PDM converges quickly to a target value at around  $1 \times 10^5$  collocation points although the convergence rate of the PDM is slightly slower than that of the FDM. The initial slow convergence rates at the small number of nodes sets apparently seem to be responsible for this slower rate.

#### 4.4 Solidification with interior boundary

In this section, we investigate a solidification containing two inclusions represented by ellipsoid solid phases. The presence of inclusions is a common occurrence during solidification processes such as conventional casting, laser melting, melt spinning, etc. (Yu and Li 2015; Xu et al. 2015). Due to the periodic boundary condition, one inclusion is separated into halves. These inclusions act as interior boundary and barrier for grain growth. In this example, instead of generating additional collocation points to track arbitrary behaviors of the inclusions, the surfaces of the inclusions are interpolated with collocation points that capture the shape of ellipsoid (Fig. 11). This dramatically simplifies the moving interface modeling without loss of computational accuracy.

As the inclusions are assumed to be chemically stable and the liquid metal cannot be transformed into the inclusions, the phase-field variables associated with the inclusions remain unchanged during the solidification process. Similarly, the nodal positions that describe the surfaces of inclusion are maintained. To observe the morphology around the inclusion more

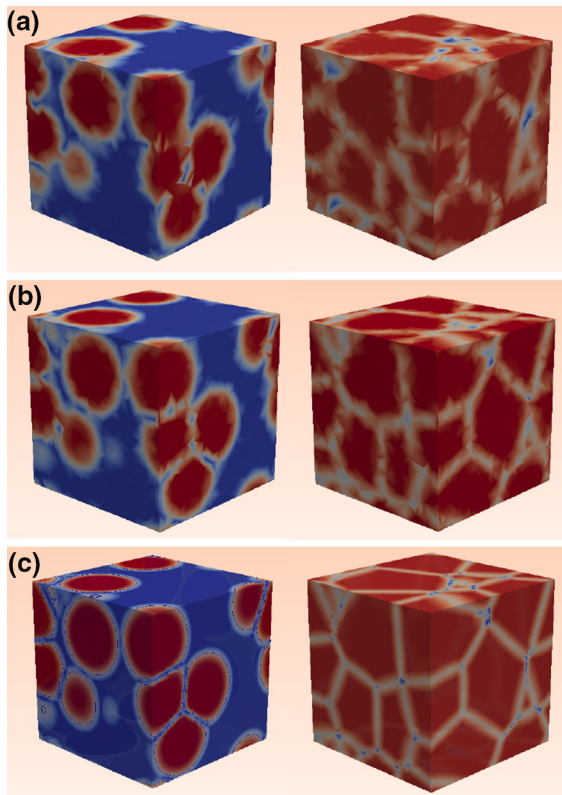


**Fig. 9** Comparison of the microstructural evolution at  $400 \Delta t$  (left column) and  $1600 \Delta t$  for different levels of discretizations **a** 31,250 collocation points, **b** 125,000 collocation points, and **c** 500,000 collocation points

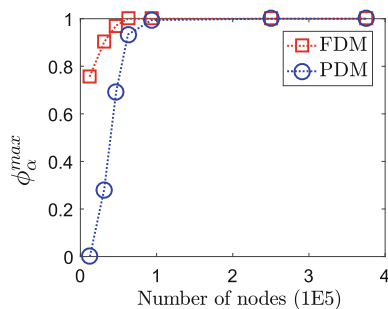


**Fig. 10** Convergence of computed phase-field variable at an arbitrarily chosen collocation point

clearly, a cross-sectional cut through the left inclusion is presented in Fig. 11b. The microstructural evolutions for this case are displayed in Fig. 12, where only the inclusion isosurface is shown in all of the time snapshots. It is obvious that the inclusions remain stable as planned while the remaining liquid metal undergoes solidification. Grain boundaries can be

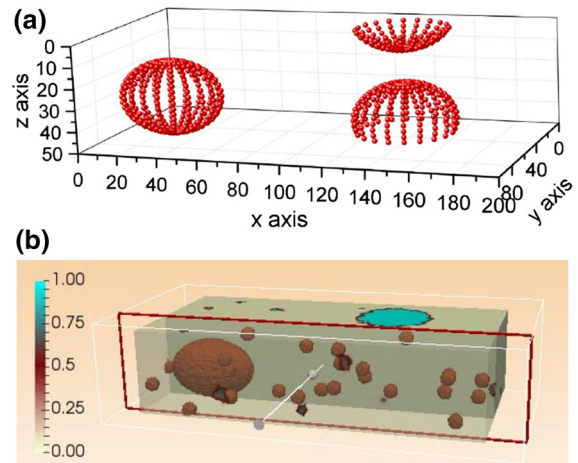


**Fig. 11** **a** Nodal distribution on the surface of two inclusions and **b** demonstration of the cross-section cut through the simulation domain

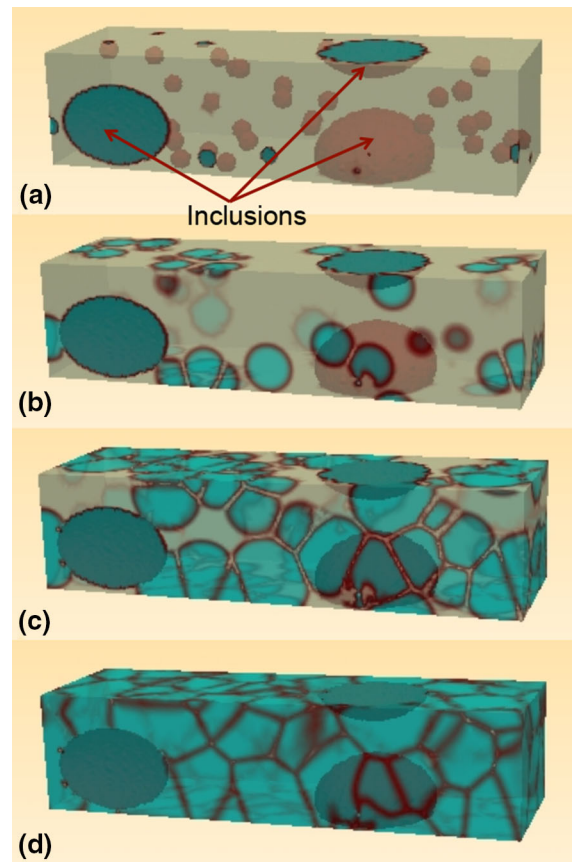


**Fig. 12** Microstructural evolution in systems with inclusion simulated by PDM **a** initial state, at **b**  $4000 \Delta t$  **c**  $8000 \Delta t$  and **d**  $20,000 \Delta t$

clearly identified from Fig. 12 and no penetration of other grains into the inclusions is observed.

This example with the ellipsoid inclusions demonstrates the flexibility of the PDM because freely placed collocation points on curved and complex surfaces might not be easily described in the framework of uniform distributions of the collocation points. At the same time, for the case of evolving interfaces related to intricate structures, the nodal density and positions can be adaptively adjusted according to the gradient of phase-field variables. This allows more collocation points to be concentrated where a phase-field variable changes drastically. Additional issues on the resolution of the evolving intricate interfaces with an adaptive discretization technique will be addressed in our future work.

## 5 Conclusions

The performance of the PDM was verified through solving phase-field solidification problems without or with intricate geometrical features and higher-order derivatives. It was established that the PDM can easily handle the high-order derivatives in the strong form formulation for a given governing partial differential equation. It does not require numerical integration and is easy to apply of problems with complex geometries since it only utilizes the collocation points and their neighboring sets with properly controlled support radius. Also, the variable support radius is quite appropriate for the local nodal refinement and dynamic adaptivity.

From the viewpoint of the strong form formulation based on the Taylor expansion, the numerical implementation of the PDM is similar to that of the FDM because partial differential equations are directly transformed into their discrete counterparts with the aid of the particle derivative approximation. The shape function and its derivative approximations up to the order of consistency, which is essential for discretizing the governing equations, are obtained at the off-line stage for a given uniform or random distributions of the collocation points. Then, the shape function and the derivative approximations are freely used at the on-line stage in the form of the particle derivative approximation. The topological difficulty in modeling the geometrically complex interface causing fatal problems in the conventional numerical schemes was

successfully resolved by the diffusive interface approach combined with the PDM.

To improve the computation efficiency and facilitate the large-scale problem simulation, parallelization of the developed code is implemented by integrating the PETSC library. It was shown that the parallel efficiency is increased at the off-line stage and the highest efficiency is obtained when the number of collocation points per processor is around 4000. On the other hand, as the number of processors increases at the on-line stage, the efficiency is reduced due to communication time required among the processors at every timestep.

Finally, the robustness and reliability of the PDM are demonstrated by solving a coupled phase-field and temperature evolution equation describing the polycrystalline solidification of Ni. Excellent agreement among three approaches, i.e., the FDM and the PDM with uniform and random distributions of the collocation points, was found for this problem related to the simulation for the morphological evolution during solidification process. Moreover, the level of discretization shows a minor influence on the prediction results. The remarkable similarity of the results was achieved even with the number of collocation points decreasing by a factor of 16.

In our future work, a *hp*-adaptivity algorithm will be incorporated into the PDM framework to efficiently solve the diffusive moving interface problems with complex interface geometry and other challenging problems involving higher-order derivatives.

**Acknowledgements** The first and fifth authors acknowledge support by the Office of Naval Research (ONR) through the 2016 ONR Summer Faculty Research Fellowship and the Naval Research Laboratory's core funding, respectively.

## References

- Aluru, N.R.: A point collocation method based on reproducing kernel approximations. *Int. J. Numer. Meth. Eng.* **47**, 1083–1121 (2000)
- Amiri, F., Millán, D., Arroyo, M., Silani, M., Rabczuk, T.: Fourth order phase-field model for local max-ent approximants applied to crack propagation. *Comput. Methods Appl. Mech. Eng.* **312**, 254–275 (2016)
- Amiri, F., Millán, D., Shen, Y., Rabczuk, T., Arroyo, M.: Phase-field modeling of fracture in linear thin shells. *Theor. Appl. Fract. Mech.* **69**, 102–109 (2014)

- Anitescu, C., Jia, Y., Zhang, Y.J., Rabczuk, T.: An isogeometric collocation method using superconvergent points. *Comput. Methods Appl. Mech. Eng.* **284**, 1073–1097 (2015)
- Areias, P., Msekh, M.A., Rabczuk, T.: Damage and fracture algorithm using the screened poisson equation and local remeshing. *Eng. Fract. Mech.* **158**, 116–143 (2016b)
- Areias, P., Rabczuk, T., Msekh, M.A.: Phase-field analysis of finite-strain plates and shells including element subdivision. *Comput. Methods Appl. Mech. Eng.* **312**, 322–350 (2016c)
- Areias, P., Rabczuk, T., de Sá, J.C.: A novel two-stage discrete crack method based on the screened poisson equation and local mesh refinement. *Comput. Mech.* **58**(6), 1003–1018 (2016a)
- Balay, S., Abhyankar, S., Adams, M.F., Brown, J. Brune, P., Buschelman, K., Dalcin, L., Eijkhout, V., Gropp, W.D., Kaushik, D., Knepley, M.G., McInnes, L.C., Rupp, K., Smith, B.F., Zhang, H., Zhang, H.: PETSc Web page. Smith, Stefano Zampini (2016)
- Balay, S., Abhyankar, S., Adams, M.F., Brown, J. Brune, P., Buschelman, K., Dalcin, L., Eijkhout, V., Gropp, W.D., Kaushik, D., Knepley, M.G., McInnes, L.C., Rupp, K., Smith, B.F., Zhang, H., Zhang, H.: PETSc users manual. Technical Report ANL-95/11 - Revision 3.7, Argonne National Laboratory (2016)
- Belytschko, T., Lu, Y.Y., Gu, L.: Element-free Galerkin method. *Int. J. Numer. Meth. Eng.* **37**, 229–256 (1994)
- Boettinger, W.J., Warren, J.A., Beckermann, C., Karma, A.: Phase-field simulation of solidification. *Annu. Rev. Mater. Res.* **32**(1), 163–194 (2002)
- Ceniceros, H.D., N  s, R.L., Roma, A.M.: Three-dimensional, fully adaptive simulations of phase-field fluid models. *J. Comput. Phys.* **229**(17), 6135–6155 (2010)
- Chen, L.Q.: Phase-field models for microstructure evolution. *Annu. Rev. Mater. Res.* **32**(1), 113–140 (2002)
- Du, Q., Zhang, J.: Analysis of a mixed finite element method for a phase field bending elasticity model of vesicle membrane deformation. *J. Comput. Math.* **24**(3), 265–280 (2006)
- Du, Q., Zhang, J.: Adaptive finite element method for a phase field bending elasticity model of vesicle membrane deformations. *SIAM J. Sci. Comput.* **30**(3), 1634–1657 (2008)
- Eiken, J., B  ttger, B., Steinbach, I.: Multiphase-field approach for multicomponent alloys with extrapolation scheme for numerical application. *Phys. Rev. E* **73**, 066122 (2006)
- Fried, E., Gurtin, M.E.: Continuum theory of thermally induced phase transitions based on an order parameter. *Physica D* **68**, 326343 (1993)
- Fu, Y., Michopoulos, J.G., Song, J.H.: Bridging the multi-phase field model with the molecular dynamics for the solidification of nano-crystals. *J. Comput. Sci.* **20**, 187–197 (2017) (submitted)
- Gomez, H., Calo, V.M., Bazilevs, Y., Hughes, T.J.R.: Isogeometric analysis of the Cahn-Hilliard phase-field model. *Comput. Methods Appl. Mech. Eng.* **197**(4950), 4333–4352 (2008)
- Gurtin, M.E., Fried, E.: Dynamic solid-solid transitions with phase characterized by an order parameter. *Physica D* **72**, 287308 (1994)
- Gurtin, M.E., Fried, E.: A phase-field theory for solidification based on a general anisotropic sharp-interface theory with interfacial energy and entropy. *Physica D* **91**, 143181 (1996)
- Huerta, A., Vidal, Y., Villon, P.: Pseudo-divergence-free element free galerkin method for incompressible fluid flow. *Comput. Methods Appl. Mech. Eng.* **193**, 11191136 (2004)
- Jiang, W., Kim, T.-Y.: Spline-based finite-element method for the stationary quasi-geostrophic equations on arbitrary shaped coastal boundaries. *Comput. Methods Appl. Mech. Eng.* **299**, 144–160 (2016)
- Kaminsky, A.: BIG CPU, BIG DATA: Solving the World’s Toughest Computational Problems with Parallel Computing, chapter Strong Scaling. Rochester Institute of Technology, Rochester (2015)
- Karma, A.: Phase-field formulation for quantitative modeling of alloy solidification. *Phys. Rev. Lett.* **87**, 115701 (2001)
- Kim, D.W., Kim, Y.: Point collocation methods using the fast moving least-square reproducing kernel approximation. *Int. J. Numer. Meth. Eng.* **56**(10), 1445–1464 (2003)
- Kim, D.W., Kim, H.K.: Point collocation method based on the FMLSRK approximation for electromagnetic field analysis. *IEEE Trans. Magn.* **40**, 1029–1032 (2004)
- Kim, S.G., Kim, D.I., Kim, W.T., Park, Y.B.: Computer simulations of two-dimensional and three-dimensional ideal grain growth. *Phys. Rev. E* **74**, 061605 (2006)
- Kim, D.W., Liu, W.K., Yoon, Y.C., Belytschko, T., Lee, S.H.: Meshfree point collocation method with intrinsic enrichment for interface problems. *Comput. Mech.* **40**, 1037–1052 (2007a)
- Kim, T.-Y., Park, E.-J., Shin, D.-W.: A  $C^0$ -discontinuous galerkin method for the stationary quasi-geostrophic equations of the ocean. *Comput. Methods Appl. Mech. Eng.* **300**, 225–244 (2016)
- Kim, D.W., Yoon, Y.C., Liu, W.K., Belytschko, T.: Extrinsic meshfree approximation using asymptotic expansion for interfacial discontinuity of derivative. *J. Comput. Phys.* **221**, 370–394 (2007b)
- Krongauz, Y., Belytschko, T.: Consistent pseudo-derivatives in meshless methods. *Comput. Methods Appl. Mech. Eng.* **146**, 371–386 (1997)
- Krongauz, Y., Belytschko, T.: A petrov-galerkin diffuse element method (PG DEM) and its comparison to EFG. *Comput. Mech.* **19**, 327–333 (1997)
- Lan, C.W., Chang, Y.C.: Efficient adaptive phase field simulation of directional solidification of a binary alloy. *J. Cryst. Growth* **250**(34), 525–537 (2003)
- Lee, S.H., Yoon, Y.C.: Meshfree point collocation method for elasticity and crack problems. *Int. J. Numer. Meth. Eng.* **61**(1), 22–48 (2004)
- Li, S., Liu, W.K.: Synchronized reproducing kernel interpolant via multiple wavelet expansion. *Comput. Mech.* **21**, 28–47 (1998)
- Li, S., Liu, W.K.: Reproducing kernel hierarchical partition of unity, Part I-formulation and theory. *Int. J. Numer. Meth. Eng.* **45**, 251–288 (1999)
- Li, S., Liu, W.K.: Meshfree and particle methods and their applications. *Appl. Mech. Rev.* **55**, 1–34 (2002)
- Liu, W.K., Jun, S., Zhang, Y.: Reproducing kernel particle methods. *Int. J. Numer. Methods Fluids* **20**, 1081–1106 (1995)
- Lowengrub, J.S., R  tz, A., Voigt, A.: Phase-field modeling of the dynamics of multicomponent vesicles: spinodal

- decomposition, coarsening, budding, and fission. *Phys. Rev. E* **79**, 031926 (2009)
- Moelans, N., Blanpain, B., Wollants, P.: An introduction to phase-field modeling of microstructure evolution. *Calphad* **32**(2), 268–294 (2008)
- Monaghan, J.J.: Smoothed particle hydrodynamics. *Ann. Rev. Astron. Astrophys.* **30**, 543–574 (1992)
- Nayroles, B., Touzot, G., Villon, P.: Generalizing the finite element method: diffuse approximation and diffuse elements. *Comput. Mech.* **10**, 307–318 (1992)
- Onate, E., Idelsohn, S., Zienkiewicz, O.C., Taylor, R.L.: Finite point method in computational mechanics. Applications to convective transport and fluid flow. *Int. J. Numer. Meth. Eng.* **39**, 3839–3866 (1996a)
- Onate, E., Idelsohn, S., Zienkiewicz, O.C., Taylor, R.L., Sacco, C.: A stabilized finite point method of analysis of fluid mechanics problems. *Comput. Methods Appl. Mech. Eng.* **139**, 315–346 (1996b)
- Onate, E., Perazzo, F., Miquel, J.: A finite point method for elasticity problems. *Comput. Struct.* **79**, 2151–2163 (2001)
- Peco, C., Rosolen, A., Arroyo, M.: An adaptive meshfree method for phase-field models of biomembranes. Part II: a lagrangian approach for membranes in viscous fluids. *J. Comput. Phys.* **249**, 320–336 (2013)
- Rosam, J., Jimack, P.K., Mullis, A.: A fully implicit, fully adaptive time and space discretisation method for phase-field simulation of binary alloy solidification. *J. Comput. Phys.* **225**(2), 1271–1287 (2007)
- Rosolen, A., Peco, C., Arroyo, M.: An adaptive meshfree method for phase-field models of biomembranes. Part I: approximation with maximum-entropy basis functions. *J. Comput. Phys.* **249**, 303–319 (2013)
- Steinbach, I.: Phase-field models in materials science. *Modell. Simul. Mater. Sci. Eng.* **17**(7), 073001 (2009)
- Steinbach, I., Pezzolla, F.: A generalized field method for multiphase transformations using interface fields. *Physica D* **134**(4), 385–393 (1999)
- Steinbach, I., Pezzolla, F., Nestler, B., Seelberg, M., Prieler, R., Schmitz, G., Rezende, J.: A phase field concept for multiphase systems. *Physica D* **94**, 135–147 (1996)
- Tan, Z., Lim, K.M., Khoo, B.C.: An adaptive mesh redistribution method for the incompressible mixture flows using phase-field model. *J. Comput. Phys.* **225**(1), 1137–1158 (2007)
- Thornton, K., Ågren, J., Voorhees, P.W.: Modelling the evolution of phase boundaries in solids at the meso- and nano-scales. *Acta Mater.* **51**(19), 5675–5710 (2003)
- Wise, S., Kim, J., Lowengrub, J.: Solving the regularized, strongly anisotropic cahn-hilliard equation by an adaptive nonlinear multigrid method. *J. Comput. Phys.* **226**(1), 414–446 (2007)
- Xu, Y., Wu, Y.G., Zhang, C.J., Zhu, L.G.: Precipitation and growth of inclusions in solidification process of steel. *J. Iron. Steel Res. Int.* **22**(9), 804–811 (2015)
- Yoon, Y.C., Lee, S.H., Belytschko, T.: Enriched meshfree collocation method with diffuse derivatives for elastic fracture. *Comput. Math. Appl.* **51**, 1349–1366 (2006)
- Yoon, Y.C., Song, J.H.: Extended particle difference method for weak and strong discontinuity problems: part I. Derivation of the extended particle derivative approximation for the representation of weak and strong discontinuities. *Comput. Mech.* **53**(6), 1087–1103 (2014a)
- Yoon, Y.C., Song, J.H.: Extended particle difference method for weak and strong discontinuity problems: part II. Formulations and applications for various interfacial singularity problems. *Comput. Mech.* **53**(6), 1105–1128 (2014b)
- Yoon, Y.C., Song, J.H.: Extended particle difference method for moving boundary problems. *Comput. Mech.* **54**(3), 723–743 (2014c)
- Yu, H.S., Li, L.G.: Size distribution of inclusions in 12% cr stainless steel with a wide range of solidification cooling rates. *Int. J. Miner. Metall. Mater.* **22**(11), 1157–1162 (2015)
- Yue, P., Zhou, C., Feng, J.J., Ollivier-Gooch, C.F., Hu, H.H.: Phase-field simulations of interfacial dynamics in viscoelastic fluids using finite elements with adaptive meshing. *J. Comput. Phys.* **219**(1), 47–67 (2006)
- Zhu, J., Chen, L.Q., Shen, J., Tikare, V.: Coarsening kinetics from a variable-mobility cahn-hilliard equation: application of a semi-implicit fourier spectral method. *Phys. Rev. E* **60**, 3564–3572 (1999)